ACS Partner Journal

ARTIFICIAL PHOTOSYNTHESIS

pubs.acs.org/artificialphotosynthesis

Article

Cobalt-Loaded Carbon Nitride Demonstrates Enhanced Photocatalytic Production of H_2 from Lignocellulosic Biomass Components

Mitchell Beckedorf, Jenna Holland, and Robert Godin*

Cite This: *Artif. Photosynth.* 2025, 1, 50–62

Read Online

ACCESS | Metrics & More | Article Recommendations | Supporting Information

ABSTRACT: Photocatalytic production of hydrogen (H_2) from biomass is a promising avenue for advancing sustainable energy generation. We prepared carbon nitride (CN_x) with cobalt (Co) as an oxidation cocatalyst (denoted CN_x/Co) to improve photocatalytic H_2 production through photoreforming components of lignocellulosic biomass under visual light irradiation. CN_x/Co was synthesized by loading Co onto preformed CN_x through a straightforward thermal deposition. The thermal loading of Co at 450 °C led to the formation of a mixed valence CoO_x, which shifted Co^{2+} character to Co^{3+} over the course of the hydrogen evolution reaction (HER). Compared to CN_x without Co, our materials with 0.3 and 0.6 wt % Co demonstrate twice the apparent quantum yield (AQY) for H_2 production under irradiation at 405 nm using glucose as a sacrificial electron donor (3.0% and 2.8%, respectively, vs 1.4%). Time-resolved spectroscopic investigations indicate that the Co extracts charges in the subnanosecond time scale and promotes the formation of beneficial long-lived charges. Impressively, some photocatalytic activity is observed when using the robust polymers of cellulose and lignin as the oxidation substrates (0.2 and 0.1% AQY, respectively). The ability to oxidize abundant biomass without extensive prepreparation is promising for waste upcycling applications.

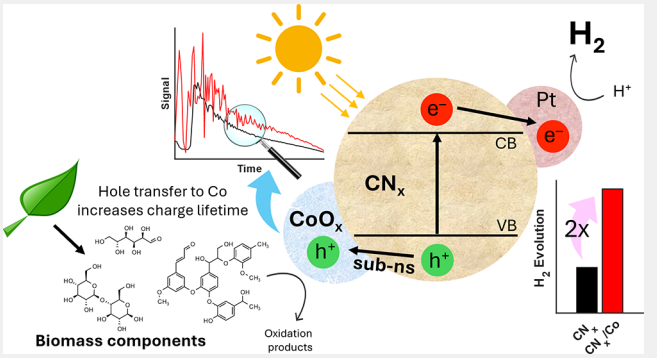

KEYWORDS: *carbon nitride, cobalt oxide, biomass valorization, photocatalytic hydrogen production, time-resolved spectroscopy*

INTRODUCTION

With the global population surpassing eight billion people as of 2023,[1] addressing the world's energy crisis is more urgent than ever. Despite efforts to shift reliance from carbon-based fuels to renewable resources, fossil fuels continue to dominate the energy sector, accounting for 82% of yearly demands and resulting in 39.2 gigatons of carbon dioxide (CO_2) produced annually.[2] Hydrogen (H_2) is a promising green energy vector due in part to its clean combustion with only water as a product and provides three times more energy than gasoline per unit mass.[3] However, conventional methods of H_2 generation, such as steam methane reforming, offer only a marginal reduction in emissions.[4] Photocatalysis stands out as a favorable technique of generating green H_2, leveraging nonexhaustible solar energy and converting it into a storable and readily accessible chemical form.[5] While efficient water splitting is necessary to make a closed loop process, the kinetic and thermodynamic challenges of the water oxidation half-reaction have proven to be a formidable barrier.[6] In response, the employment of lignocellulosic biomass as a sacrificial agent in the photocatalytic process has emerged as a potential solution to both the challenges of water oxidation and the valorization of an agricultural byproduct generated on the order of 100 gigatons annually.[7,8] As global agricultural demands surge to accommodate the growing population, feedstocks with low nutritional merit, such as rice straw, sugar cane bagasse, and corn stover, have been identified as sources of alternative energy due to their high carbohydrate content and natural abundance.[9] This has sparked an effort to recover waste and integrate these raw materials into the circular economy.[10]

Carbon nitride (CN_x) is an organic, low cost, chemically and thermally stable semiconductor with a suitable band structure for visible light response and is a promising candidate for many green photocatalytic processes, including CO_2 reduction, pollutant degradation, and H_2 production.[11−13] Due to a facile synthesis from abundant precursors, CN_x has established itself as a principal environmentally friendly and nontoxic hetero-

Received: May 1, 2024
Revised: August 12, 2024
Accepted: August 23, 2024
Published: September 2, 2024

geneous photocatalyst. Although the effectiveness of pristine CN_x is limited by rapid charge recombination and low surface area, techniques including synthetic modifications to CN_x morphology, formation of heterojunctions, and doping with organic or inorganic elements have been demonstrated to improve the photocatalytic efficiency of CN_x.[14−17] However, these materials often require lengthy synthetic procedures and expensive or toxic reagents to fabricate, limiting their applied utility.[18]

Surface modification with cocatalyst heterojunctions serving as electron or hole trap centers are a proven modification strategy to improve the photocatalytic capabilities of CN_x by reducing surface charge recombination and/or speeding up the kinetics of redox reactions.[19−21] A wealth of studies have demonstrated enhanced efficiency of the hydrogen evolution reaction (HER) or oxygen evolution reaction (OER) by engineering CN_x surface heterostructures with noble metals, forming a Schottky barrier.[22−26] Platinum (Pt) in particular is established as an effective reduction cocatalyst due to its low Fermi level and high electrochemical activity and has been shown to increase H_2 production capabilities of CN_x through the reduction of aqueous protons.[27,28] Recently, highly active iridium (Ir)-based catalyst complexes and cocatalysts have been demonstrated as impressive facilitators of the difficult OER.[29−31] However, the high cost and low natural abundance of noble metals limit the practicality of these systems. A shift to the use of Earth abundant elements is required for sensible upscaling of CN_x heterojunction photosystems.[32] In response, cobalt (Co) as a competent oxidation cocatalyst has been employed to enhance photocatalytic activity of CN_x in a variety of states, including cobalt sulfide,[33] cobalt-phenanthroline,[34] and mesoporous CN_x with cobalt oxide,[35] for H_2 production, with easily oxidized triethanolamine (TEOA) as a hole scavenger. However, to achieve the more challenging oxidation of the chemically robust biomass, holes must be substantially long-lived to outlast the slow kinetics of charge transfer. Notably, the demonstration of a simple synthetic strategy of adding active Co to CN_x to produce efficient systems for the photocatalytic valorization of the biomass is still lacking.

Co incorporation onto semiconductors TiO_2 and $ZnIn_2S_4$ from a simple thermal deposition of $Co(NO_3)_2$ has been exhibited to promote efficient photogenerated charge separation, increasing rates of photocatalytic H_2 evolution in the presence of methanol or TEOA respectively.[36,37] Motivated by these reports, we explored the capability of Co, incorporated into preformed CN_x from urea through a simple thermal deposition of the precursor $Co(NO_3)_2$, as an oxidation cocatalyst to improve photocatalytic production of H_2 using various biomass components as sacrificial electron donors. CN_x with a range of Co loadings (denoted CN_x/Co) was prepared and characterized through Fourier-transform infrared spectroscopy (FTIR), X-ray diffraction (XRD), and X-ray photoelectron spectroscopy (XPS). The weight percentage (wt %) of Co in synthesized CN_x/Co samples was confirmed with inductively coupled plasma optical emission spectroscopy (ICP-OES). Transmission electron microscopy (TEM), bright- and dark-field scanning TEM (BF/DF-STEM) with energy-dispersive X-ray spectroscopy (EDS) elemental mapping, and high-angle annular dark-field (HAADF) STEM were utilized to explore the Co distribution on the CN_x surface. The photocatalytic activity was determined with respect to a variety of components of lignocellulosic biomass, including glucose, xylose, arabinose, cellulose, and lignin. Myo-inositol and dextran were included as sacrificial electron donors of study for the purpose of clarifying the reaction mechanism. The end products of the photodegradation of glucose were analyzed by high-performance liquid chromatography (HPLC). Finally, we examined the optical properties and charge carrier dynamics of CN_x/Co through ultraviolet−visible diffuse reflectance spectroscopy (UV−vis DRS), steady state and time-resolved photoluminescence (ssPL and trPL), and transient absorbance spectroscopy (TAS).

EXPERIMENTAL SECTION

Materials. Acetonitrile (ACN), α-cellulose, Amberlite IR-120 (H^+ form) anion exchange resin, chloroplatinic acid hexahydrate ($H_2PtCl_6{\cdot}6H_2O$), D-gluconic acid sodium salt, hydrochloric acid (HCl), and urea were obtained from Sigma-Aldrich. Cobalt nitrate hexahydrate ($Co(NO_3)_2{\cdot}6H_2O$) and sodium hydroxide (NaOH) were sourced from VWR Chemicals. D-(−)-Arabinose, D-(+)-xylose, lignin (alkaline), and potassium hydroxide (KOH) were purchased from TCI. D-(+)-Glucose (dextrose) was obtained from Fischer Scientific. Myo-inositol was purchased from Alfa Aesar. Dextran was sourced from Carbosynth. Ultrapure water was obtained from a Millipore system. All chemicals were of reagent grade or higher.

Synthesis of CN_x. Urea was ground with a mortar and pestle until a fine uniform powder was achieved. Four g of ground urea were loaded into covered alumina crucibles and heated at 550 °C for 4 h with a ramp rate of 2 °C min^{-1}. After natural cooling, the resulting crude product was ground with water and purified through successive washings of H_2O, 1 M KOH, 1 M HCl, ACN, H_2O, 1 M KOH, 1 M HCl, and H_2O in 50 mL conical tubes. Each washing step consisted of 5 min of sonication followed by 10 min of centrifugation at 4000 rpm to isolate the solid. The solid product was air-dried for 12 h following the final wash and separation.

Synthesis of CN_x/Co. The Co cocatalyst was incorporated into pristine CN_x through thermal deposition. $Co(NO_3)_2{\cdot}6H_2O$ was ground in an aqueous dispersion of pristine CN_x with a mortar and pestle. The crude mixture was allowed to dry while being stirred on a hot plate at 60 °C for 24 h. The dry product was ground again, loaded in covered alumina crucibles, and heated to 450 °C for 1 h with a ramp rate of 2 °C min^{-1}. The resulting products were labeled $CN_x/Co_{0\%}$, $CN_x/Co_{0.3\%}$, $CN_x/Co_{0.6\%}$, $CN_x/Co_{1.9\%}$, or $CN_x/Co_{3.1\%}$, indicating the wt % of Co added to the mass of CN_x.

Material Characterization. FTIR spectroscopy measurements of the solid powders were taken with a Thermo Electron Nicolet 6700 spectrometer with a SmartOrbit diamond attenuated total reflection (ATR) attachment and an XT-KBr beamsplitter.

XPS spectra were obtained by a nanoFAB (University of Alberta) through a Kratos Axis Ultra spectrometer with monochromatized Al Kα ($h\nu$ = 1486.71 eV) at ambient room temperature. A binding energy of 84.0 eV of Au $4f_{7/2}$ with reference to the Fermi level was used to calibrate the spectrometer. The pressure of the analysis chamber was maintained at $>5 \times 10^{-10}$ Torr. High resolution measurements were taken with a hemispherical electron-energy analyzer working at a pass energy of 20 eV. The survey spectra was acquired within a 0−1100 eV binding energy range at an analyzer pass energy of 160 eV. Charge effects were corrected by calibrating to the C 1s peak at 284.8 eV. XPS spectra were

https://doi.org/10.1021/aps.4c00007
Artif. Photosynth. 2025, 1, 50−62

fitted using custom written MATLAB software (https://github.com/SolarSpec/XPSfitting). Shirley backgrounds were applied to subtract the inelastic background of the core-level peaks. The full width at half-maximum (fwhm) of the Voigt peaks (generated from 90% Gaussian and 10% Lorentzian line shapes) were determined by examining the uniqueness plots[38] across a range of fwhm for all samples. The fwhm values chosen were fixed for the fitting of all samples, allowing for variations of 10% for C 1s, N 1s, and O 1s spectra, 30% for Pt 4f spectra, and 60% for Co 2p (to fit the satellite).

XRD data collection was performed at nanoFAB (University of Alberta) using a Bruker D8 Discover Powder X-ray diffractometer purchased from Bruker AXS, Madison, U.S.A. It was equipped with a Cu X-ray target, with an operating voltage of 40 kV and 30 mA, and with a Centric Eulerian Vertical Cradle for the basic powder stage or DHS 900 heating stage. Data was collected with a focused beam, a 5° soller slit, fixed divergence slit of 0.6 (or 0.3), and a 1D mode LynxEYE detector with a nickel K-β filter. Scan type was Locked Couple, the increment was 0.03, and the scan range 20−90° with a speed of 2° min^{-1} or 0.5 step s^{-1}.

ICP-OES data were collected at the Fipke Laboratory of Trace Element Research (FiLTER, University of British Columbia) on a Thermo iCAP 6000 series ICP spectrometer. In-house quality control standards were run in a 1% HNO_3 matrix. CN_x/Co samples were digested in concentrated H_2SO_4 and diluted to 3% H_2SO_4 with 1% HNO_3. The Co emission wavelength was monitored at 228.6 nm.

TEM, BF/DF-STEM with EDS elemental mapping, and HAADF STEM analysis were conducted at nanoFAB (University of Alberta) on a JEOL JEM-ARM200cF S/TEM equipped with a cold field-emission gun and probe spherical aberration corrector and operated at a 200 kV accelerating voltage.

Hydrogen Evolution Reaction. Photocatalytic activity was determined through HER with biomass derivatives as sacrificial agents. We tested glucose, xylose, arabinose, cellulose, lignin, myo-inositol, and dextran. An alkaline solution was prepared with 10 mL of 5 M NaOH and 100 mg of the sacrificial agent of interest and sonicated for 5 min. Twenty mg of CN_x/Co and 84 μL of H_2PtCl_6 solution (to give 3 wt % Pt with respect to CN_x) were added, and the solution was sonicated for 5 min before transfer to a 16 mL quartz cuvette. The cuvette was sealed with a silicone septum and 3D printed plastic O-ring to achieve more complete sealing, placed in a photoreactor, and purged for 10 min with argon (Ar). The solution was stirred at 400 rpm for the entire course of the reaction. The Pt cocatalyst was photodeposited on CN_x/Co through irradiation in the reaction mixture with a 405 nm light emitting diode (LED) with a power density of 20 mW cm^{-2}. Following 1 h of irradiation, the solution was purged for 10 min with Ar to remove all H_2. The solution was then irradiated for 30 min, after which the partial pressure of H_2 in the headspace of the cuvette generated an electrochemical current measured with a Unisense Clarke-electrode H_2 microsensor. Current was converted to a voltage readout by a Unisense Microsensor Multimeter. Detector response was converted to% partial pressure through a two-point calibration curve under 0 and 2% volume H_2 atmospheres. The calibration measurements were taken in the headspace of a 16 mL cuvette filled with 10 mL of water under a gas flow of Ar (for the 0% H_2) or a certified 2% H_2 gas mixture (balance N_2). To expedite the slow rate of equilibration of H_2 between the solution and headspace resulting from the small surface of the air−liquid interface, the cuvette was thoroughly shaken before each reading. The percentage of H_2 in the 6 mL headspace was converted to a molar value in the headspace using the Ideal Gas Law and was further used to calculate the concentration of H_2 in the 10 mL solution through Henry's Law (Henry's constant for H_2 in water at 298.15 K of 7.8×10^{-6} mol/m^3·Pa).[39] The amounts of H_2 in the headspace and in solution were summed to quantify total H_2 in the cuvette following 30 min of irradiation. Errors bars on the AQY represent the standard error from multiple trials. Sample calculations can be found in the Supporting Information (eqs S1−S9).

Characterization of the Photocatalytic Degradation Products. The products of the photocatalytic decomposition of glucose were resolved using a Waters HPLC system with a refractive index detector (Waters 2414) and a Hypercarb porous graphitic carbon column (Thermo Scientific, 100 mm × 2.1 mm). Ten μL of supernatant was injected with water as the mobile phase at an isocratic flow rate of 0.3 mL min^{-1} for 15 min. The detector was equilibrated at 30 °C. To obtain the samples for analysis, the HER was performed as stated above with the following modifications: 100 mL of NaOH, 1 g of glucose, 200 mg of $CN_x/Co_{0.6\%}$, and 840 μL of H_2PtCl_6 were reacted in a 100 mL round-bottom flask sealed with a rubber septum. Following the reaction, H_2 in the flask headspace was measured to confirm that the reaction had proceeded, after which the reaction mixture was centrifuged to isolate the photocatalyst. The supernatant was separated by gravity filtration. Amberlite 120-IR anion exchange resin (H^+ form) was used to batch neutralize the strongly alkaline supernatant, which was stored in the dark at 2 °C until analysis. One mL aliquots of supernatant were spiked with 40 μL of 500 mg/mL glucose or gluconic acid for spike analysis.

Optical Spectroscopy. Powder samples were sandwiched between a glass microscope slide and a top quartz cover slide for spectroscopic measurements.

UV−vis DRS spectra were collected by using a 50 mm OceanOptics integrating sphere and a Maya2000Pro spectrometer in conjunction with a DH-2000 OceanOptics deuterium/halogen UV−vis-NIR lamp. $BaSO_4$ was prepared in identical fashion to CN_x samples and used as a reference reflection standard.

A Horiba Scientific Fluorolog-QM fluorimeter was used to obtain ssPL spectra and trPL decays. The excitation light was set to 375 nm for steady state acquisitions. The pulsed excitation light source was 405 nm for time-resolved decays, which were monitored in the CN_x emission region at 450 nm. All measurements were taken with samples positioned at 60° relative to the detector. A sample of $BaSO_4$ was used to measure the instrument response function (IRF) of the trPL setup.

TAS kinetics and spectra were obtained by a homemade setup. A Surelight continuum Nd:YAG laser (1064 nm) was frequency tripled to generate laser pulses at 355 nm (fluence of 100 μJ cm^{-2}) and used to excite samples. A 95 W broadband Oriel lamp probe beam was focused on the sample and directed to a photodiode through Thorlabs bandpass filters (fwhm of 70−100 nm) and an Oriel Cornerstone monochromator through a series of parabolic mirrors and focusing lenses. The photodiode response was amplified by a FEMTO DHPCA-100 variable gain high-speed current amplifier, and the resulting voltage signal was filtered by custom electronics. The signal was averaged over 128−512 scans from 550−950 at

https://doi.org/10.1021/aps.4c00007
Artif. Photosynth. 2025, 1, 50−62

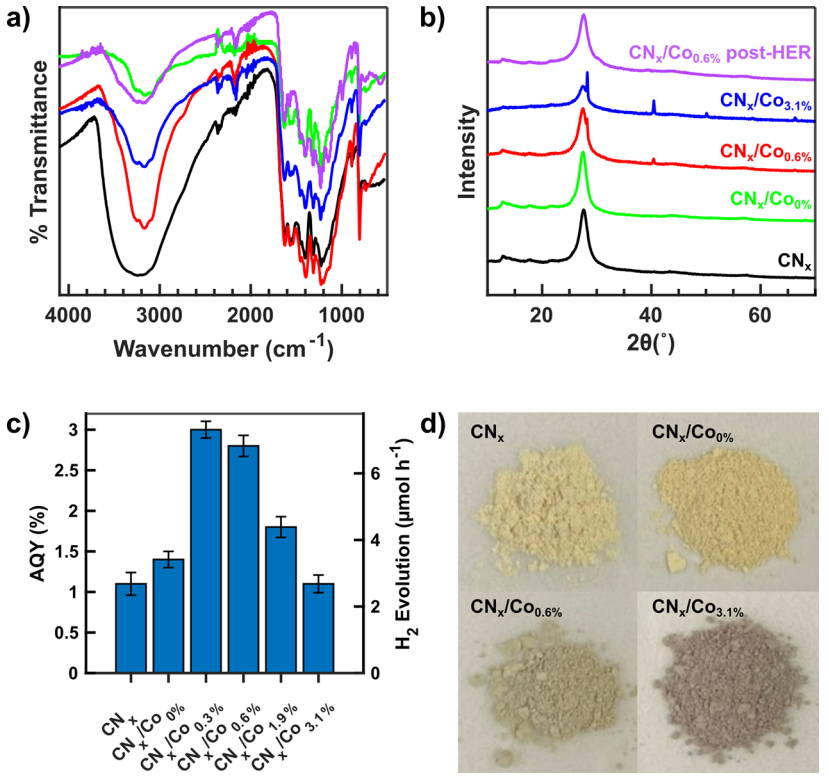

Figure 1. (a) FTIR spectra of CN_x, $CN_x/Co_{0\%}$, $CN_x/Co_{0.6\%}$, $CN_x/Co_{3.1\%}$, and $CN_x/Co_{0.6\%}$ after 30 min of HER. Legend in panel (b) also applies to panel (a). (b) XRD patterns of CN_x, $CN_x/Co_{0\%}$, $CN_x/Co_{0.6\%}$, $CN_x/Co_{3.1\%}$, and $CN_x/Co_{0.6\%}$ after 30 min of HER. (c) Photocatalytic activity of all CN_x/Co materials measured as the AQY and H_2 evolution rate, using glucose as a sacrificial agent and 3 wt % Pt loading. (d) Photographs of CN_x and CN_x/Co powders.

50 nm intervals. Data were acquired with custom LabVIEW code and processed with MATLAB code available at https://github.com/SolarSpec/SpectraBuilder. No unexpected safety hazards were encountered during the experimental procedures.

RESULTS AND DISCUSSION

Characterization. We prepared CN_x from urea as a precursor material due to its reported high photocatalytic activity and surface area when compared to CN_x prepared from dicyandiamide (DCDA), melamine, or thiourea.[40,41] Co was incorporated into prepared CN_x through grinding and thermal deposition at 450 °C using 0, 0.3, 0.6, 1.9, and 3.1 wt % with respect to the mass of CN_x. Products were labeled $CN_x/Co_{y\%}$, where the y denotes the wt % of Co.

FTIR, XRD, and XPS data were collected to confirm the structure of CN_x in our material and to observe the chemical environment of Co. The FTIR spectra for CN_x, $CN_x/Co_{0\%}$, $CN_x/Co_{0.6\%}$, and $CN_x/Co_{3.1\%}$ are displayed in Figure 1a (legend in Figure 1b also applies to 1a), along with the pattern of $CN_x/Co_{0.6\%}$ recovered from the reaction mixture after Pt photodeposition and a 30 min HER run (denoted $CN_x/Co_{0.6\%}$ post-HER). All species exhibit the characteristic heptazine (tri-s-triazine) out-of-plane bending vibration shift at approximately 800 cm^{-1}.[42] Peaks from 1000−1800 cm^{-1} are telling of the C−N and C═N bonds in nitrogen-containing heterocyclic compounds.[43] A prominent band observed at roughly 3200 cm^{-1} by N−H (or O−H stretching in H_2O) further confirms the structure of CN_x in all samples.[22] We attribute the difference in band intensity at 3200 cm^{-1} to residual moisture, and no other significant differences are discernible in the spectra of pristine CN_x compared to the Co loaded samples. The $CN_x/Co_{0.6\%}$ post-HER spectra remain analogous to those of all other species. As such, we conclude that the CN_x chemical structure is not disrupted by Co loading or during the HER.

XRD patterns for CN_x, $CN_x/Co_{0\%}$, $CN_x/Co_{0.6\%}$, and $CN_x/Co_{3.1\%}$ are displayed in Figure 1b, along with the pattern of $CN_x/Co_{0.6\%}$ recovered from the reaction mixture after Pt photodeposition and a 30 min HER (denoted $CN_x/Co_{0.6\%}$ post-HER). All species display a prominent peak at approximately 2θ = 27.5° attributed to the (002) plane formed by the interlayer $\pi-\pi$ stacking of individual CN_x sheets.[44] This peak is seen to broaden with increased addition of Co, the extent of which was quantified by measuring the full width at half-maximum (fwhm) obtained through fitting the peak to a Lorentzian shape (Figure S1). Peak sharpness in XRD patterns are representative ordered crystal structures, with sharper peaks indicating more uniform organization.[45] The (002) peak in $CN_x/Co_{0\%}$ displays a fwhm of 1.65° which increases to 1.89° and 1.92° for $CN_x/Co_{0.6\%}$ and $CN_x/Co_{3.1\%}$ respectively, suggesting the addition of Co disrupts the uniformity of interlayer stacking. Additionally, all species display a peak at 2θ = 12.9° for the (100) plane, a manifestation of intralayer heptazine repeats within sheets.[46] These peaks decrease in intensity with Co loading, further agreeing with the disruption of crystallinity brought about by Co loading.

Additional prominent peaks are observed at 28.3, 40.5, 50.1, 58.9, 66.3, and 73.6° exclusively in the pre-HER Co loaded samples, increasing in intensity as the Co loading increases. When compared to the XRD patterns of common Co oxides in the literature, we do not see agreement between our patterns

https://doi.org/10.1021/aps.4c00007
Artif. Photosynth. 2025, 1, 50−62

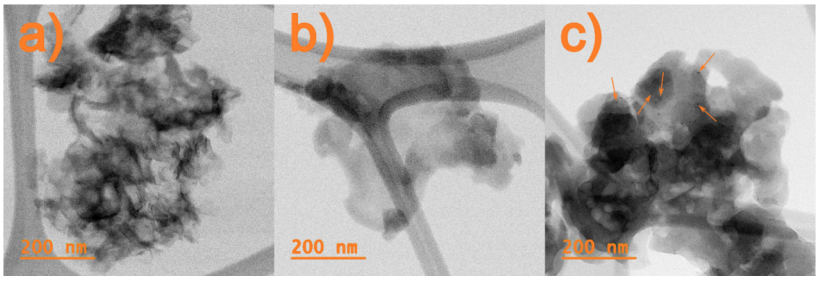

Figure 2. Bright-field (BF)-STEM micrographs of (a) $CN_x/Co_{0\%}$, (b) $CN_x/Co_{0.6\%}$, and (c) $CN_x/Co_{0.6\%}$ post-HER. Orange arrows in (c) highlight a few Pt nanoparticles.

and the patterns of CoO, $Co(OH)_2$, CoOOH, Co_2O_3, or Co_3O_4.[47−51] For comparison, neat $Co(NO_3)_2$ was calcinated at 450 °C, resulting in the distinct XRD pattern of Co_3O_4 (Figure S2). This discrepancy suggests that the CN_x substrate plays a role in the cobalt oxide formation for CN_x/Co, likely through Co−N interactions, and impedes the formation of Co_3O_4.

The XRD pattern of $CN_x/Co_{0.6\%}$ post-HER displays a change of Co environment from the shift of the prominent 2θ = 28.9° peak to a reduced intensity shoulder seen at 30.0° (Figure S3), along with new peaks seen at 34.3° and 39.3°. These transformations do not align with previously reported XRD patterns of Pt nanoparticles,[52] but instead allude to a changed Co coordination state over the course of the HER, beginning to resemble Co_2O_3 or Co_3O_4, which were investigated further.

Further insights into the chemical environments in the samples were obtained by XPS analyses. The survey scans (Figure S4) confirm the presence of carbon (C), nitrogen (N), and oxygen (O) elements in all CN_x samples. In the $CN_x/Co_{0.6\%}$ post-HER, additional sodium (Na) peaks are prominent as a result of exposure to NaOH aqueous solution. The C 1s and N 1s spectra of all CN_x samples (Figures S5 and S6) have the same features and are consistent with previous reports.[53,54] For the C 1s spectra, peaks are observed at approximately 284.8 eV (C−C, adventitious carbon), 286.5 eV (C−O, surface adsorbed species), 288.2 eV (dominant, N=C−N within the triazine ring), and 289.1 eV (C=O, surface adsorbed species). Features at higher binding energies (293 and 296 eV) are assigned to π excitation shakeup bands. For the N 1s spectra, a dominant peak is observed around 398.7 eV (C−N=C, pyridine nitrogen within the triazine unit) with two smaller features at 399.9 eV ($N-C_3$, central heptazine tertiary nitrogen) and 401.2 eV ($C-NH_x$, terminal amino group).[55,56]

The O 1s spectra (Figure S7) are also consistent with previous reports, showing two peaks at roughly 531.6 and 533.0 eV, assigned to hydroxyl (OH) groups from chemisorbed species and/or adsorbed carbonate species.[57] The $CN_x/Co_{0.6\%}$ post-HER sample shows an additional peak at 535.7 eV, which is assigned to the Na Auger peak. The relative intensities of the 531.6 and 533.0 eV peaks become similar, likely a result of the sample being put in contact with water and changing the adsorbed O-containing species. Overall, no significant changes are seen in the C 1s, N 1s, and O 1s XPS spectra across the CN_x samples, agreeing with the acquired FTIR data that the incorporation of Co did not alter the CN_x chemical composition.

As expected, $CN_x/Co_{0\%}$ shows no signal in the Co 2p region (Figure S8). Peaks are clearly observed at higher Co loadings in the $CN_x/Co_{3.1\%}$ sample. Peaks are fitted at 780.7, 782.2, 786.3, and 791.2 eV, and satellite peaks at higher binding energies are also observed. Compared to the $Co(NO_3)_2$ precursor, the lowest binding energy peak is shifted to lower values by 0.8 eV and the shoulder at 786 eV is less prominent but still clearly visible, indicating the presence of Co^{2+}. The calcined neat $Co(NO_3)_2$ give spectra entirely consistent with that of Co_3O_4,[58] and we notice that the shoulder at 786 eV is subdued (Figure S9). These are consistent with a mixed valence Co^{2+}/Co^{3+} oxide in the CN_x/Co, with a significantly greater proportion of Co^{2+} additionally suggested by the greater similarities in Co binding energies to $Co(OH)_2$ compared to Co_3O_4.[58,59] A Co 2p signal can be seen in the $CN_x/Co_{0.6\%}$ samples both before and after HER, but the signal-to-noise ratio is too low to consider the fits reliable. We can still observe a +0.3 eV shift in the lowest binding energy peak and that the Co^{2+} satellite at approximately 786 eV is less prominent after the HER (Figure S10). Both observations point to a greater proportion of Co^{3+} after the HER.

Finally, Pt is also seen in the $CN_x/Co_{0.6\%}$ post-HER sample (Figure S11), confirming the photodeposition of Pt as cocatalyst. The Pt 4f spectrum shows major peaks corresponding to Pt^0 (70.8 and 74.0 eV) and Pt^{2+} (72.4 and 75.8 eV), with an approximate 3.3 eV shift between the Pt $4f_{7/2}$ and $4f_{5/2}$ signals. The small peak at 77.7 eV might be indicative of a small amount of Pt^{4+} or a satellite. Based on the relative areas of the signals, the Pt^0/Pt^{2+} ratio is 1:1.4. These results are consistent with the reduction of the Pt^{2+} precursor to Pt nanoparticles on the surface of CN_x.[60]

BF-STEM analysis (Figure 2) and EDS elemental mapping (with corresponding DF-STEM micrographs, Figure S12) unveil homogeneously dispersed Co in $CN_x/Co_{0.6\%}$ with no clear signatures of defined nanoparticles. Both Co and Pt are displayed in the EDS mapping of $CN_x/Co_{0.6\%}$ post-HER (Figures S12 and S13). Nanoparticles with diameters of approximately 3 nm are visualized in BF/DF-STEM micrographs and HAADF STEM images (Figure S14) exclusively for $CN_x/Co_{0.6\%}$ post-HER, linking them to photodeposited Pt. Lattice spacings of the nanoparticles were determined by applying an inverse Fast Fourier Transform (iFFT) to the region of interest and calculating the average distance between the local maxima. Lattice fringes are 2.4 ± 0.04 Å apart, consistent with previously reported *d*-spacing distances of the (111) plane of Pt.[61,62]

Photocatalytic Activity. Pt was photodeposited as a reduction cocatalyst from H_2PtCl_6 by irradiating CN_x/Co and deaerated glucose solution with a 405 nm LED (20 mW cm^{-2}) for 1 h. The dispersion was then purged with Ar and irradiated again for 30 min to determine the HER activity and H_2 evolution from the amount of H_2 in the cuvette. Glucose has been shown to be a hole acceptor when employed with oxide

https://doi.org/10.1021/aps.4c00007
Artif. Photosynth. 2025, 1, 50−62

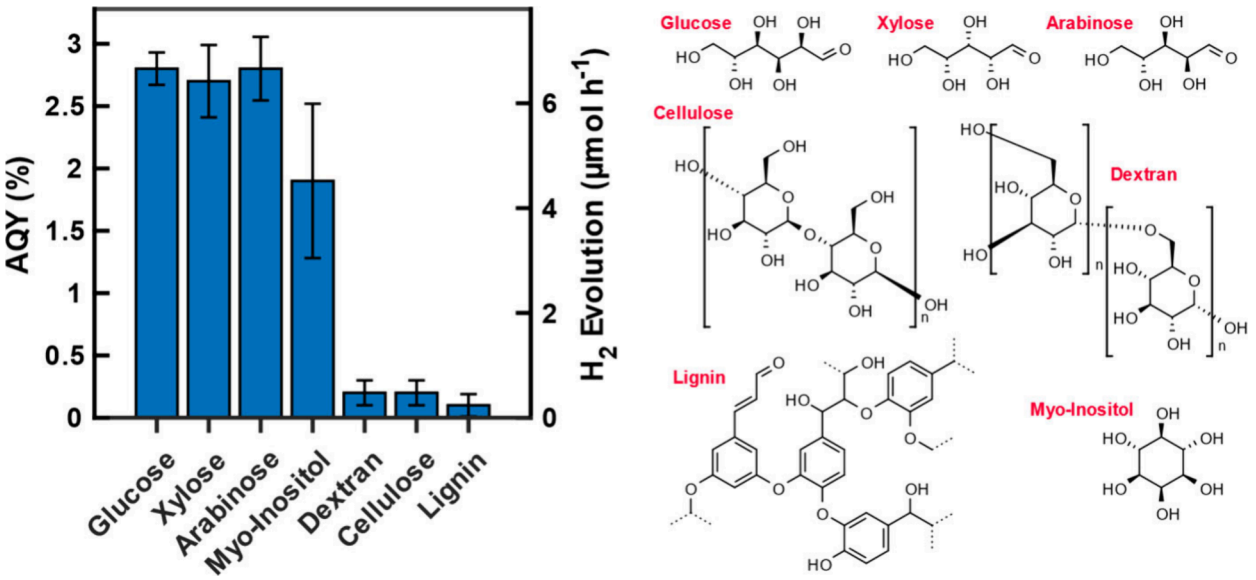

Figure 3. Photocatalytic activity of $CN_x/Co_{0.6\%}$ with glucose, xylose, arabinose, myo-inositol, dextran, cellulose, or lignin as scavengers. Chemical structures of sacrificial agents are displayed on the right using the linear depiction for the monosaccharides.

based photocatalysts for the production of H_2,[63,64] but limited success has been found using glucose with CN_x based materials due to the restricted interfacial charge transfer between glucose and poorly dispersed pristine CN_x.[65] However, glucose undergoes pH-dependent confirmational changes which, in an alkaline environment, increase electrostatic interaction between CN_x and glucose.[66] Additionally, glucose oxidation is shown to be more favorable in alkaline conditions.[67,68] Therefore, following HER tests with 1, 5, and 10 M NaOH (Figure S15), all following experimentation was conducted in 10 mL of 5 M NaOH as the optimal solvent conditions.

We measured the HER activity of the sample series with glucose and calculated the AQY and H_2 evolution (Figure 1c). Of the Co-loaded samples, $CN_x/Co_{0.3\%}$ and $CN_x/Co_{0.6\%}$ displayed the highest activity of 3.0 and 2.8% AQY (H_2 evolution of 7.3 and 6.8 μmol h^{-1}), respectively, followed by $CN_x/Co_{1.9\%}$ and $CN_x/Co_{3.1\%}$ with respective AQY values of 1.8 and 1.1% (4.4 and 2.6 μmol h^{-1}). We suggest the decreased activity of the CN_x/Co species with higher Co loadings is due to a high concentration of Co blocking the limited active sites present on CN_x or through shading the photocatalyst, reducing photon absorption.[69,70] $CN_x/Co_{0.3\%}$ and $CN_x/Co_{0.6\%}$ impressively displayed twice or greater the photocatalytic activity of $CN_x/Co_{0\%}$ and pristine CN_x, which exhibited AQYs of 1.4 and 1.1% (3.5 and 2.7 μmol h^{-1}) respectively. The sample with 0.6% Co was chosen for detailed spectroscopy over the similar high activity 0.3% Co sample to increase the likelihood of observing spectral signatures attributed to the Co. $CN_x/Co_{0.6\%}$ was chosen for further investigation of activity with other model components of biomass to be consistent with the samples studied by optical spectroscopy (*vide infra*).

Lignocellulosic biomass, comprised of polymers of cellulose, hemicellulose, and lignin, forms intricate nonuniform structures that commonly undergo separative pretreatments before being processed into value-added materials.[71] Cellulose is a linear polymer of glucose monomers joined by β-1,4 glycosidic bonds and is cross-linked by hemicellulose chains comprised of various pentose and hexose sugars, including glucose, xylose, and arabinose. The complex structure of lignin, comprised of a heterogeneous array of monolignols, further reinforces cellulose.[72] As such, we elected to use the polymers cellulose and lignin, as well as the monosaccharides glucose, xylose, and arabinose as models of postprocessed biomass. The glucose polymer dextran was chosen as a model branched polymer saccharide, consisting of linear α-1,6 glycosidic bonds between monomers with branched α-1,3 linkages.[73] Additionally, the cyclic polyol (often referred to as "sugar alcohol") myo-inositol was selected for mechanistic investigation due to its lack of carbonyl group, where oxidation readily occurs in monosaccharides.

As displayed in Figure 3a, the monosaccharides glucose, xylose, and arabinose demonstrate superior photocatalytic activity (2.8, 2.7, and 2.8% AQY respectively) when compared to all other sacrificial agents. The analogous activity of these sugars reflect their structural similarity, signifying a common mechanism of oxidation. Changing to myo-inositol as the scavenger resulted in a slightly lower AQY of 1.9%, showing that alcohol groups can be oxidized successfully, and that carbonyl or aldehyde functional groups are not strictly necessary. As expected, use of polymers cellulose, lignin, and dextran exhibited lower activity (0.2, 0.1, and 0.2% AQY respectively), attributed to the low concentration of accessible oxidizable moieties because of insolubility or low solubility.

When preparing the alkaline solutions of CN_x/Co and biomass component, it was observed that glucose, xylose, arabinose, and myo-inositol were completely soluble in solution following 5 min of sonication. However, even when subjected up to 15 min of sonication, the polymers of cellulose, lignin, and dextran never fully dissolved. The undissolved amalgamation rapidly settled to the bottom of the cuvette despite constant stirring, where it was not in the light path and would not contribute to scavenging activity. Furthermore, the addition and sonication of lignin resulted in a deep brown colored solution. The absorbance spectrum of the 10 mg mL^{-1} solution of lignin in 5 M NaOH displayed strong absorbance at the excitation wavelength of 405 nm (Figure S17). Under 0.1% of 405 nm light was transmitted through the 1 cm path length (eq S10), severely impeding light absorption by CN_x/Co. Therefore, the observed photocatalytic activity with lignin as a hole scavenger is remarkable, attributed to irradiating CN_x/Co

https://doi.org/10.1021/aps.4c00007
Artif. Photosynth. 2025, 1, 50−62

particles near the front face of the cuvette and suggests a much greater internal quantum yield than the observed AQY.

To ascertain that H_2 photoproduction was a result of biomass photo-oxidation, control trials were performed with $CN_x/Co_{0.6\%}$ (Figure S15b). In the absence of a sacrificial agent, no H_2 production was measured. In addition, HERs were performed without 405 nm irradiation with glucose, cellulose, and lignin. Trace amounts of H_2 were detected in all "dark" reactions (0.031−0.078 μmol), attributed to exposure to ambient room light when setting up the reaction, shaking the cuvette, and taking measurements of headspace gas. The ratio of H_2 measured without and with LED irradiation was 2.3 and 10.5% for the HER trial of glucose and cellulose, respectively (Table S2). With lignin as a scavenger, the amount of H_2 produced without light was more substantial, at 50% of that produced with light. While this could suggest a non-photocatalytic degradation process, the measurements were close to the detection limit of the sensor and would be affected by small baseline shifts between calibration and the HER measurement.

The stability of the photocatalyst was evaluated by repeating multiple HER trials on the same sample. Following each HER, a new septum was used to seal the flask, which was purged again with Ar for 10 min before the next 30 min of reaction. As displayed in Figure S16, the activity of $CN_x/Co_{0.6\%}$ decreased after the first trial; however, it stayed stable at approximately two-thirds of the initial activity during the second and third trials. The performance decline may be attributed to a loss of Co during the HER. ICP-OES measurements were conducted on all CN_x/Co samples to confirm the final yield of Co present. As displayed in Table S1, an average of 67% of the measured Co is retained in the final product. However, the wt % Co in $CN_x/Co_{0.6\%}$ post-HER is significantly lower than that of $CN_x/Co_{0.6\%}$ prior to the HER (0.10% vs. 0.51%, respectively). While the wt % Co decreases by about a factor of 5, activity only diminished by less than a factor of 2, suggesting that the Co lost is not part of the most active sites. This loss of Co is likely due to interactions with the strongly alkaline solvent, sonication during preparatory steps, and mechanical abrasion from constant stirring during the reaction. Changes in the Co chemical environment as indicated by the post-HER XRD pattern, attributed to hole accumulation on Co pushing oxidation toward Co^{3+}, may also play a role in the decreased activity. Despite the decline in photocatalytic activity following the first HER cycle, the stabilized activity remains nearly twice that of pristine CN_x (as shown in Figures 1 and S16). While this stable activity demonstrates the potential of our current system, future work should aim to enhance the robustness of the Co cocatalyst.

Steady State Optical Spectroscopy. UV−vis DRS and ssPL spectra were analyzed to examine the optical properties of our samples. The diffuse reflectance spectra were transformed to absorbance-like spectra using the Kubelka−Munk function as illustrated in Figure 4a. When compared to pristine CN_x, the samples that underwent the additional thermal treatment exhibit a red shift of approximately 20 nm in the absorbance edge, including $CN_x/Co_{0\%}$ with no Co. Using Tauc plots analyzed by a multivariate adaptive regression splines algorithm,[74] direct band gap energies of 3.04, 2.91, 2.92, and 2.88 eV were determined for pristine CN_x, $CN_x/Co_{0\%}$, $CN_x/Co_{0.6\%}$, and $CN_x/Co_{3.1\%}$, respectively (Figure S18). These observations contrast the blueshift in the absorption edge typically seen in CN_x thermally treated to fabricate nanosheets,

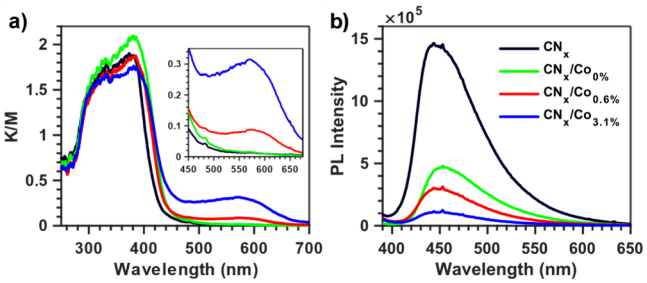

Figure 4. UV−vis DRS (a) and ssPL (b) spectra of CN_x, $CN_x/Co_{0\%}$, $CN_x/Co_{0.6\%}$, and $CN_x/Co_{3.1\%}$. Legend in panel (b) applies to all panels. Panel (a) inset: zoomed-in x axis to highlight the absorbance peak attributed to Co.

resulting in a larger bandgap when compared to pristine CN_x.[22,75] We conclude that the nanosheet structure was not obtained from our 450 °C thermal treatment process, as we used lower temperatures compared to those commonly described in the literature (around 550 °C). However, structural defects were likely introduced through the thermal treatment, leading to a red shift in the absorbance edge.[76,77] Striking is the intensified absorption at approximately 570 nm, shown to increase linearly with the wt % Co loading (Figure S19). This peak is indicative of a tetrahedrally coordinated Co^{2+} environment[78,79] and supports the presence of Co^{2+} in the mixed CoO_x oxide. Comparing the spectra of $CN_x/Co_{0.6\%}$ before and post-HER (Figure S20), we see a decrease in the prominence of the 570 nm band, consistent with some oxidation of Co^{2+} species to Co^{3+}. Additional absorption is also seen post-HER due to the photodeposited Pt.[80]

A significant decrease in fluorescence intensity between pristine CN_x and $CN_x/Co_{0\%}$ is observed (Figure 4b) and aligns the introduction of structural defects which tend to increase nonradiative recombination.[77] A further decrease in PL intensity is observed in the Co loaded samples suggesting improved charge carrier separation.[76] The reduction in PL intensity is near-linear with greater Co loading (Figure S21), suggesting that the addition of Co delays the recombination of electron−hole pairs.[43] However, it is possible that the lower PL intensity for samples with Co is a result of the absorption of excitation or emission light by the Co oxide, leading us to use time-resolved spectroscopic techniques to distinguish between the different possibilities.

Time-Resolved Spectroscopy. For more detailed information regarding the charge carrier dynamics, we performed TAS at μs−ms time scales on $CN_x/Co_{0\%}$, $CN_x/Co_{0.6\%}$, and $CN_x/Co_{3.1\%}$. Samples were excited at 355 nm, and transient absorptance data were acquired from 550−950 nm in 50 nm increments. The TAS spectra (Figure 5) display the change between the ground and excited state absorption as a function of wavelength at a range of time slices. Spectral shapes provide evidence toward the identity of photogenerated charges.[15] It has previously been determined that positive absorption features in the visible and near-infrared (NIR) wavelengths of CN_x, a n-type semiconductor, are attributed to excited state electrons.[81,82] Therefore, comparing spectral contours of $CN_x/Co_{0\%}$ to those of Co-loaded materials can classify the excited state species attributed to Co addition. When we compare, for example, the shape of the spectra measured at 1 ms normalized to the absorptance at 700 nm (Figure S22), we see a similar spectral shape among all three materials. We accordingly

https://doi.org/10.1021/aps.4c00007
Artif. Photosynth. 2025, 1, 50−62

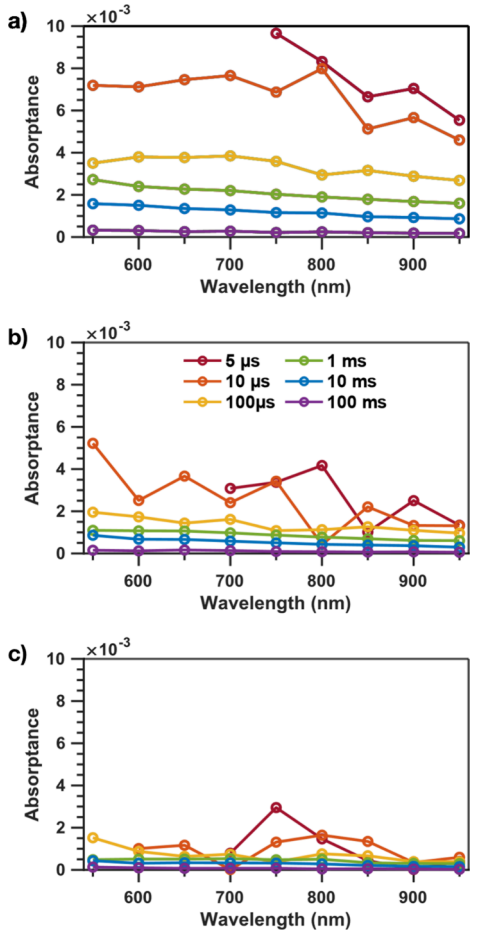

Figure 5. Transient absorbance spectra of (a) $CN_x/Co_{0\%}$, (b) $CN_x/Co_{0.6\%}$, and (c) $CN_x/Co_{3.1\%}$, monitored from 550 to 950 nm in 50 nm increments, at 5 μs to 100 ms time scales. Legend in (b) applies to all figures.

conclude that we are monitoring electrons in CN_x as charge carriers in all spectra.

The kinetic decays allow us to study the time dependence of photogenerated electron behavior on the μs−ms time scale. The log(absorptance) vs. log(time) plot of the kinetic decay of $CN_x/Co_{0\%}$ monitored at 700 nm displays a linear decay curve (Figure S23), signifying that charge recombination in $CN_x/Co_{0\%}$ follows power law decay kinetics as described by the multiple charge trapping/detrapping model.[83] The power law exponents (Table S3) describe α, and can be used to calculate the energetic distribution of trap states in organic semiconductors (E_c, Equation S11). The α and E_c values are within 21% of each other, suggesting that the addition of Co does not alter the energetic trap state distribution.

As displayed by the decays normalized at 10 μs (Figure S24), the decay half-life ($t_{50\%}$), the amount of time it takes for the signal intensity to decrease by half from its maximum, belongs longer with Co addition. The extracted $t_{50\%}$ values (Tables 1 and S4) further highlight the increased charge carrier lifetime which increase by factors of 1.5−3.5 for $CN_x/Co_{0.6\%}$ and 5.2−14.7 for $CN_x/Co_{3.1\%}$ when compared to $CN_x/Co_{0\%}$. These data are in line with charge extraction to Co, slowing down charge recombination from increased spatial separation.[32]

The TAS signal amplitude decreases significantly with the addition of Co (Figures S25 and S26). As the signal is attributed to electrons, this signal decrease is at odds with the idea that the Co is an oxidation cocatalyst and accepts holes. Since the oxidation activity of the CN_x/Co samples does indeed increase, we instead attribute the TAS signal decrease to absorption of the excitation light by the CoO_x. It seems likely that the decrease in ssPL intensity with increased Co loading can at least partially also be attributed to absorption of excitation light. A more significant decrease in signal amplitude is seen for TAS (Table 1), consistent with stronger CoO_x absorption at the TAS excitation wavelength (355 nm) compared to the ssPL excitation wavelength (375 nm).

We further conducted trPL measurements for additional insights in the charge carrier dynamics (Figure 6). The decay

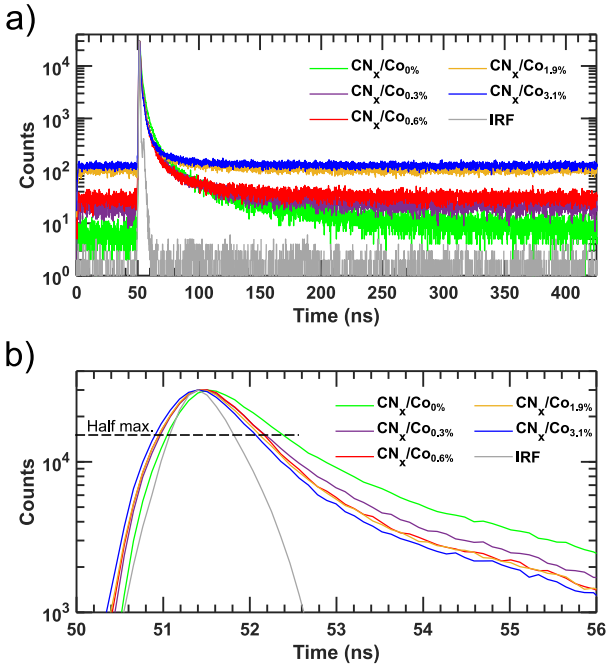

Figure 6. trPL decays of CN_x/Co samples with (a) full-axes view and (b) zooming into the initial decay.

of $CN_x/Co_{0\%}$ was well fitted by a power law decay convolved with the IRF function (Figure S28). Like the TAS, the power law model is consistent with charge carrier dynamics that undergo multiple trapping and release. The power law parameter obtained from the fit was 1.75 (Table S5). A

Table 1. Comparison of Selected Optical Signals Observed for CN_x/Co with ssPL, TAS, and trPL

		TAS signal amplitude relative to $CN_x/Co_{0\%}$		TAS $t_{50\%}$ relative to $CN_x/Co_{0\%}$		
	ssPL intensity relative to $CN_x/Co_{0\%}$	600 nm	900 nm	600 nm	900 nm	trPL exponential component contribution
$CN_x/Co_{0.6\%}$	64%	35%	23%	3.5	1.7	33%
$CN_x/Co_{3.1\%}$	26%	14%	6%	14.7	5.6	37%

https://doi.org/10.1021/aps.4c00007
Artif. Photosynth. 2025, 1, 50−62

power law exponent of 1.5 was previously observed and had good agreement with a model describing thermal equilibrium between emissive and nonemissive states.[82] Our increased value of 1.75 could be indicative of a nonthermalized charge distribution since our measurements were on the faster ns time scale compared to the μs−ms time scale previously analyzed.

With the addition of Co, the trPL decays accelerate, as indicated by the $t_{50\%}$ values that decrease from 0.98 to 0.69 ns with increasing Co loading (Table S5). The shortening of the $t_{50\%}$ is consistent with charge extraction by the Co. Quantitative fits of the trPL decays of the Co-loaded samples were obtained from a model with an exponential component in addition to the fixed power law component determined for $CN_x/Co_{0\%}$ (Figures S29−S32). The additional exponential component corresponds to the charge transfer process to Co. Exponential lifetimes of 0.18−0.28 ns are recovered, which we consider an estimate as they are significantly shorter than the IRF width of approximately 0.8 ns. Together with the $t_{50\%}$ decrease, the trPL measurements reveal a subns charge transfer from CN_x to Co that can kinetically compete with deactivation pathways.

The relative emission of the exponential component is linked to the proportion of emissive CN_x states that are deactivated by charge transfer. We note that the contribution from the exponential component increases from 22% to 37% when the Co loading is increased from 0.5% to 5% (Figure S27). The increase is under 2-fold, much smaller than the 10-fold increase in Co loading, and there is little change when increasing the Co loading beyond 1%. This observation suggests that the majority of charge extraction sites are already covered by Co at a 1% loading. Further increases in Co loading do not significantly improve the charge extraction efficiency but would shade or block reactive sites, explaining the decrease in the photocatalytic efficiency past 1% loading.

Mechanistic Investigation. Comparing the yields of H_2 from various scavengers with trends observed through time-resolved spectroscopy, we can comment on the photo-reforming mechanism. Irradiation with 405 nm photons generates photoexcited electrons in CN_x/Co which accumulate at surface Pt, where aqueous protons (H^+) are reduced to form H_2,[84] and holes which are spatially separated by Co following subns extraction. In the case of monosaccharides, previous studies have determined the rate limiting step of photo-oxidation of glucose to be the adsorption to the catalyst surface through the C_1 oxygen.[85] Although oxidation can proceed directly from holes to deprotonated glucose or indirectly though hole-generated hydroxyl radicals, the direct route is dominant in basic environments.[86] From here, carboxylic acids are usually generated.[84,87] Based on the observed AQYs, we predict glucose, xylose, and arabinose follow a similar mechanism of degradation.

Previous studies have put forth that the reforming of cellulose initially involves decomposition into 6-carbon monomers.[88] Specifically, a report by Caravaca et al. suggested that this process is photocatalytic and dependent on hole-generated hydroxyl radicals,[89] which would further limit the rate of this step in basic conditions. As such, we can attribute the low activity of cellulose and dextran to sluggish (photo)hydrolysis resulting from poor adsorption to the active sites on CN_x/Co. As the branched polymer dextran did not demonstrate a greater AQY than that of the linear polymer cellulose, we deduce that the increased number of sites for direct oxidation made accessible through branching does not overcome the low solubility of both polymers.

In the case of polyols, previous studies dictate indirect hole transfer to be the dominant mechanism in shorter chain (2−3 carbon) polyols, resulting in aldehydes and ketones, with direct hole transfer as the dominant mechanism in longer chain (4−6 carbon) polyols, resulting in oxidative C−C cleavage forming aldehydes.[90] However, it is important to note that the preference of long-chain polyols to undergo cleavage through direct hole transfer was credited to an increased number of anchoring hydroxyl groups of linear polyols, whereas the hydroxyl groups of myo-inositol (a cyclic polyol) may not as easily interact with CN_x/Co due to steric effects. The structural complexity of lignin combined with the steric bulk of its numerous benzene rings render adsorption to the surface of heterogeneous catalysts challenging, resulting in C−O bond cleavage favorable over C−C cleavage in most systems.[46]

HPLC was employed to resolve the end products of the HER by using $CN_x/Co_{0.6\%}$ with glucose as a scavenger. The refractive index chromatogram of the neutralized supernatant from a HER solution *without* 405 nm irradiation (Figure S33) reveals two distinct peaks eluted at retention times (t_R) of 2.7 (assigned to the major product of glucose elimination in strong alkali)[91] and 3.2 min (glucose, identified *via* spike analysis), with a weak shoulder appearing at approximately 2.1 min. In comparison, the chromatogram of the neutralized reaction supernatant from the HER with 30 min of irradiation (Figure S34) displays four distinct peaks at t_R = 2.1, 2.6 (elimination product), 3.0 (glucose), and 4.8 min respectively. Peaks at t_R = 2.1 and 4.8 min are assigned to products of glucose photooxidation, and the weak shoulder at t_R = 2.1 min in the dark control can be accredited to residual light contamination on the dark sample. However, spike analysis with gluconic acid (t_R = 2.3 min), a proposed product of glucose photo-oxidation, does not align with these observed peaks. This result, coupled with the photocatalytic activity observed with myo-inositol as an electron donor, hints at some distinctions with the commonly reported mechanisms.[86,92] Further analysis is required for the precise determination of the end products and the elucidation of the mechanism.

CONCLUSION

We report that the surface heterojunction engineering of Co onto CN_x through thermal loading of $Co(NO_3)_2$ results in a mixed valence CoO_x environment. As observed through XRD, XPS, and UV−vis DRS measurements, the photocatalytic HER appears to alter the coordination environment of the initial mixed valence CoO_x, shifting from Co^{2+} toward greater Co^{3+} character. Optimal loading of 0.3−0.6% Co doubles the photocatalytic activity of CN_x in the presence of aqueous glucose and other monosaccharaides. Furthermore, the Co loaded CN_x can also photo-oxidize polysaccharides, polyols, and lignin. We attribute the observed increase of photocatalytic activity to enhanced photogenerated hole extraction and spatial surface charge separation by Co. Along with the generation of solar fuel H_2, further investigation into the oxidation products arising from the degradation of the hole acceptors is warranted to determine the full potential of our system. Many studies have demonstrated the selective production of value-added chemicals from saccharides and alcohols, such as high demand chemical precursors and biofuels, which further promote the utility of photocatalytic processes.[93,94]

https://doi.org/10.1021/aps.4c00007
Artif. Photosynth. 2025, 1, 50−62

Generation of solar fuels is a promising technique of supplying off grid power and managing the energy crisis, but many previously demonstrated systems rely on rare and expensive precursor materials to obtain favorable efficiencies. Clearly, further innovation in crafting beneficial interfaces and catalytic centers is needed before these systems can achieve commercial success. We demonstrate that Co as an earth abundant transition metal deposited on CN_x through a straightforward thermal deposition holds favorable properties as oxidation cocatalysts to enhance H_2 evolution. Continued research into other earth abundant and low valent early transition metals and organic compounds is critical to deploying sustainable photocatalytic systems.

■ ASSOCIATED CONTENT

Data Availability Statement

Data represented in the figures of the main text are available in the Federated Research Data Repository (FRDR) under DOI: 10.20383/103.01046.

Supporting Information

The Supporting Information is available free of charge at https://pubs.acs.org/doi/10.1021/aps.4c00007.

Sample calculations, extended XRD, XPS, ICP-OES, TEM, photoactivity, absorbance, photoluminescence, transient absorption spectroscopy, and HPLC data (PDF)

■ AUTHOR INFORMATION

Corresponding Author

Robert Godin − *Department of Chemistry, The University of British Columbia, Kelowna, BC V1V 1V7, Canada; Clean Energy Research Center, University of British Columbia, Vancouver, BC V6T 1Z3, Canada; Okanagan Institute for Biodiversity, Resilience, and Ecosystem Services, University of British Columbia, Kelowna, BC V1 V 1 V7, Canada;* orcid.org/0000-0001-7945-8548; Email: robert.godin@ubc.ca

Authors

Mitchell Beckedorf − *Department of Chemistry, The University of British Columbia, Kelowna, BC V1V 1V7, Canada*

Jenna Holland − *Department of Chemistry, The University of British Columbia, Kelowna, BC V1V 1V7, Canada*

Complete contact information is available at: https://pubs.acs.org/10.1021/aps.4c00007

Author Contributions

Author contributions to the work are as follows. M.B.: Data curation, formal analysis, investigation, writing−original draft, writing−review and editing. J.H.: Data curation, formal analysis, investigation. R.G.: Conceptualization, funding acquisition, project administration, supervision, writing−original draft, writing−review and editing.

Notes

The authors declare no competing financial interest.

■ ACKNOWLEDGMENTS

This work was carried out while on the unceded and traditional territory of the Syilx People of the Okanagan Nation. We are grateful for financial support from the Natural Sciences and Engineering Research Council of Canada (NSERC) and the Canada Foundation for Innovation (CFI). M.B. is grateful for support from an NSERC Undergraduate Student Research Award (USRA). We thank UBC for financial support of the Cluster of Research Excellence in Solar Energy for Net Zero. Special thanks to Dr. Wes Zandberg for thoughtful discussions on sugars and their separation. We also thank Shihong, Peng, and Xuehai of the nanoFAB facility at the University of Alberta for assistance with the XPS, XRD, and TEM measurements, and Dr. Mark Button of the Fipke Laboratory for Trace Element Research for collecting ICP-OES data.

■ REFERENCES

(1) Download 2023 World Population Data Sheet. Population Reference Bureau. https://2023-wpds.prb.org/download-files/ (accessed 2024−01−31).

(2) Institute, E. Home. Statistical review of world energy. https://www.energyinst.org/statistical-review/home (accessed 2024−02−03).

(3) Yue, M.; Lambert, H.; Pahon, E.; Roche, R.; Jemei, S.; Hissel, D. Hydrogen Energy Systems: A Critical Review of Technologies, Applications, Trends and Challenges. *Renew. Sustain. Energy Rev.* **2021**, *146*, 111180.

(4) Turner, J. A. Sustainable Hydrogen Production. *Science* **2004**, *305* (5686), 972−974.

(5) Chiarello, G. L.; Selli, E. 8 - Photocatalytic Production of Hydrogen. In *Advances in Hydrogen Production, Storage and Distribution*; Basile, A., Iulianelli, A., Eds.; Woodhead Publishing, 2014; pp 216−247. DOI: 10.1533/9780857097736.2.216.

(6) Jafari, T.; Moharreri, E.; Amin, A. S.; Miao, R.; Song, W.; Suib, S. L. Photocatalytic Water Splitting—The Untamed Dream: A Review of Recent Advances. *Molecules* **2016**, *21* (7), 900.

(7) Liu, X.; Duan, X.; Wei, W.; Wang, S.; Ni, B.-J. Photocatalytic Conversion of Lignocellulosic Biomass to Valuable Products. *Green Chem.* **2019**, *21* (16), 4266−4289.

(8) Davis, K. F.; Gephart, J. A.; Emery, K. A.; Leach, A. M.; Galloway, J. N.; D'Odorico, P. Meeting Future Food Demand with Current Agricultural Resources. *Glob. Environ. Change* **2016**, *39*, 125−132.

(9) Mujtaba, M.; Fernandes Fraceto, L.; Fazeli, M.; Mukherjee, S.; Savassa, S. M.; Araujo de Medeiros, G.; do Espírito Santo Pereira, A.; Mancini, S. D.; Lipponen, J.; Vilaplana, F. Lignocellulosic Biomass from Agricultural Waste to the Circular Economy: *A Review with Focus on Biofuels, Biocomposites and Bioplastics*. *J. Clean. Prod.* **2023**, *402*, 136815.

(10) Phiri, R.; Mavinkere Rangappa, S.; Siengchin, S. Agro-Waste for Renewable and Sustainable Green Production: A Review. *J. Clean. Prod.* **2024**, *434*, 139989.

(11) Sharma, R.; Almáši, M.; Nehra, S. P.; Rao, V. S.; Panchal, P.; Paul, D. R.; Jain, I. P.; Sharma, A. Photocatalytic Hydrogen Production Using Graphitic Carbon Nitride (GCN): A Precise Review. *Renew. Sustain. Energy Rev.* **2022**, *168*, 112776.

(12) Lu, Q.; Eid, K.; Li, W.; Abdullah, A. M.; Xu, G.; Varma, R. S. Engineering Graphitic Carbon Nitride (g-C3N4) for Catalytic Reduction of CO2 to Fuels and Chemicals: Strategy and Mechanism. *Green Chem.* **2021**, *23* (15), 5394−5428.

(13) Song, X.; Yang, Q.; Yin, M.; Tang, D.; Zhou, L. Highly Efficient Pollutant Removal of Graphitic Carbon Nitride by the Synergistic Effect of Adsorption and Photocatalytic Degradation. *RSC Adv.* **2018**, *8* (13), 7260−7268.

(14) Yang, Z.; Zhang, Y.; Schnepp, Z. Soft and Hard Templating of Graphitic Carbon Nitride. *J. Mater. Chem. A* **2015**, *3* (27), 14081−14092.

(15) Mitchell, E.; Law, A.; Godin, R. Interfacial Charge Transfer in Carbon Nitride Heterojunctions Monitored by Optical Methods. *J. Photochem. Photobiol. C Photochem. Rev.* **2021**, *49*, 100453.

(16) Zhang, W.; Xu, D.; Wang, F.; Chen, M. Element-Doped Graphitic Carbon Nitride: Confirmation of Doped Elements and Applications. *Nanoscale Adv.* **2021**, *3* (15), 4370−4387.
(17) Jiang, W.; Wang, H.; Zhang, X.; Zhu, Y.; Xie, Y. Two-Dimensional Polymeric Carbon Nitride: Structural Engineering for Optimizing Photocatalysis. *Sci. China Chem.* **2018**, *61* (10), 1205−1213.
(18) Zhurenok, A. V.; Vasilchenko, D. B.; Kozlova, E. A. Comprehensive Review on G-C3N4-Based Photocatalysts for the Photocatalytic Hydrogen Production under Visible Light. *Int. J. Mol. Sci.* **2023**, *24* (1), 346.
(19) Kumar Singh, A.; Das, C.; Indra, A. Scope and Prospect of Transition Metal-Based Cocatalysts for Visible Light-Driven Photocatalytic Hydrogen Evolution with Graphitic Carbon Nitride. *Coord. Chem. Rev.* **2022**, *465*, 214516.
(20) Guo, R.-T.; Zhang, Z.-R.; Xia, C.; Li, C.-F.; Pan, W.-G. Recent Progress of Cocatalysts Loaded on Carbon Nitride for Selective Photoreduction of CO2 to CH4. *Nanoscale* **2023**, *15* (19), 8548−8577.
(21) Zhang, G.; Lan, Z.-A.; Wang, X. Surface Engineering of Graphitic Carbon Nitride Polymers with Cocatalysts for Photocatalytic Overall Water Splitting. *Chem. Sci.* **2017**, *8* (8), 5261−5274.
(22) Niu, P.; Zhang, L.; Liu, G.; Cheng, H.-M. Graphene-Like Carbon Nitride Nanosheets for Improved Photocatalytic Activities. *Adv. Funct. Mater.* **2012**, *22* (22), 4763−4770.
(23) Zhang, Y.; Ligthart, D. A. J. M.; Quek, X.-Y.; Gao, L.; Hensen, E. J. M. Influence of Rh Nanoparticle Size and Composition on the Photocatalytic Water Splitting Performance of Rh/Graphitic Carbon Nitride. *Int. J. Hydrog. Energy* **2014**, *39* (22), 11537−11546.
(24) Samanta, S.; Martha, S.; Parida, K. Facile Synthesis of Au/g-C3N4 Nanocomposites: An Inorganic/Organic Hybrid Plasmonic Photocatalyst with Enhanced Hydrogen Gas Evolution Under Visible-Light Irradiation. *ChemCatChem.* **2014**, *6* (5), 1453−1462.
(25) Li, X.; Cui, P.; Zhong, W.; Li, J.; Wang, X.; Wang, Z.; Jiang, J. Graphitic Carbon Nitride Supported Single-Atom Catalysts for Efficient Oxygen Evolution Reaction. *Chem. Commun.* **2016**, *52* (90), 13233−13236.
(26) Christoforidis, K. C.; Fornasiero, P. Photocatalytic Hydrogen Production: A Rift into the Future Energy Supply. *ChemCatChem.* **2017**, *9* (9), 1523−1544.
(27) Dao, D. Q.; Anh Nguyen, T. K.; Kang, S. G.; Shin, E. W. Engineering Oxidation States of a Platinum Cocatalyst over Chemically Oxidized Graphitic Carbon Nitride Photocatalysts for Photocatalytic Hydrogen Evolution. *ACS Sustain. Chem. Eng.* **2021**, *9* (43), 14537−14549.
(28) Zhu, Y.; Wang, T.; Xu, T.; Li, Y.; Wang, C. Size Effect of Pt Co-Catalyst on Photocatalytic Efficiency of g-C3N4 for Hydrogen Evolution. *Appl. Surf. Sci.* **2019**, *464*, 36−42.
(29) Topchiyan, P.; Vasilchenko, D.; Tkachev, S.; Sheven, D.; Eltsov, I.; Asanov, I.; Sidorenko, N.; Saraev, A.; Gerasimov, E.; Kurenkova, A.; Kozlova, E. Highly Active Visible Light-Promoted Ir/g-C3N4 Photocatalysts for the Water Oxidation Reaction Prepared from a Halogen-Free Iridium Precursor. *ACS Appl. Mater. Interfaces* **2022**, *14* (31), 35600−35612.
(30) Gao, J.; Liu, Y.; Liu, B.; Huang, K.-W. Progress of Heterogeneous Iridium-Based Water Oxidation Catalysts. *ACS Nano* **2022**, *16* (11), 17761−17777.
(31) Bai, Y.; Li, C.; Liu, L.; Yamaguchi, Y.; Bahri, M.; Yang, H.; Gardner, A.; Zwijnenburg, M. A.; Browning, N. D.; Cowan, A. J.; Kudo, A.; Cooper, A. I.; Sprick, R. S. Photocatalytic Overall Water Splitting Under Visible Light Enabled by a Particulate Conjugated Polymer Loaded with Palladium and Iridium. *Angew. Chem., Int. Ed. Engl.* **2022**, *61* (26), No. e202201299.
(32) Wang, Y.; Liu, X.; Han, X.; Godin, R.; Chen, J.; Zhou, W.; Jiang, C.; Thompson, J. F.; Mustafa, K. B.; Shevlin, S. A.; Durrant, J. R.; Guo, Z.; Tang, J. Unique Hole-Accepting Carbon-Dots Promoting Selective Carbon Dioxide Reduction Nearly 100% to Methanol by Pure Water. *Nat. Commun.* **2020**, *11* (1), 2531.
(33) Zhou, M.; Li, L.; Zhang, S.; Yi, J.; Song, Y.; Li, H.; Xu, H. Surface Engineering of 2D Carbon Nitride with Cobalt Sulfide Cocatalyst for Enhanced Photocatalytic Hydrogen Evolution. *Phys. Status Solidi A* **2021**, *218* (10), 2100012.
(34) Zhang, J.-S.; Zhang, W.-D. Superior Photocatalytic Generation of H2 in Water Medium Through Grafting a Cobalt Molecule Co-Catalyst from Carbon Nitride Nanosheets. *ChemCatChem.* **2019**, *11* (11), 2657−2666.
(35) Kheradmand, A.; Zhu, Y.; Zhang, W.; Marianov, A.; Jiang, Y. Cobalt Oxide on Mesoporous Carbon Nitride for Improved Photocatalytic Hydrogen Production under Visible Light Irradiation. *Int. J. Hydrog. Energy* **2019**, *44* (33), 17930−17942.
(36) Xu, B.; Chong, B.; Li, H.; Yang, G. Cobalt Incorporation-Induced Photocatalytic Reactivity Enhancement in ZnIn2S4 Nanosheets for Effective Hydrogen Production. *Chem. Eng. Sci.* **2023**, *280*, 118985.
(37) Shen, H.; Ni, D.; Niu, P.; Zhou, Y.; Zhai, T.; Ma, Y. Enhancing Photocatalytic H2 Evolution from Water on CuO-Co3O4/TiO2: The Key Roles of Co3O4 Loading Amounts. *Int. J. Hydrog. Energy* **2017**, *42* (52), 30559−30568.
(38) Singh, B.; Diwan, A.; Jain, V.; Herrera-Gomez, A.; Terry, J.; Linford, M. R. Uniqueness Plots: A Simple Graphical Tool for Identifying Poor Peak Fits in X-Ray Photoelectron Spectroscopy. *Appl. Surf. Sci.* **2016**, *387*, 155−162.
(39) Sander, R. Compilation of Henry's Law Constants (Version 5.0.0) for Water as Solvent. *Atmospheric Chem. Phys.* **2023**, *23* (19), 10901−12440.
(40) Martin, D. J.; Qiu, K.; Shevlin, S. A.; Handoko, A. D.; Chen, X.; Guo, Z.; Tang, J. Highly Efficient Photocatalytic H2 Evolution from Water Using Visible Light and Structure-Controlled Graphitic Carbon Nitride. *Angew. Chem., Int. Ed.* **2014**, *53* (35), 9240−9245.
(41) Cao, S.; Yu, J. G-C3N4-Based Photocatalysts for Hydrogen Generation. *J. Phys. Chem. Lett.* **2014**, *5* (12), 2101−2107.
(42) Sunasee, S.; Leong, K. H.; Wong, K. T.; Lee, G.; Pichiah, S.; Nah, I.; Jeon, B.-H.; Yoon, Y.; Jang, M. Sonophotocatalytic Degradation of Bisphenol A and Its Intermediates with Graphitic Carbon Nitride. *Environ. Sci. Pollut. Res.* **2019**, *26* (2), 1082−1093.
(43) Chen, P.-W.; Li, K.; Yu, Y.-X.; Zhang, W.-D. Cobalt-Doped Graphitic Carbon Nitride Photocatalysts with High Activity for Hydrogen Evolution. *Appl. Surf. Sci.* **2017**, *392*, 608−615.
(44) Fina, F.; Callear, S. K.; Carins, G. M.; Irvine, J. T. S. Structural Investigation of Graphitic Carbon Nitride via XRD and Neutron Diffraction. *Chem. Mater.* **2015**, *27* (7), 2612−2618.
(45) Holder, C. F.; Schaak, R. E. Tutorial on Powder X-Ray Diffraction for Characterizing Nanoscale Materials. *ACS Nano* **2019**, *13* (7), 7359−7365.
(46) Liu, H.; Li, H.; Lu, J.; Zeng, S.; Wang, M.; Luo, N.; Xu, S.; Wang, F. Photocatalytic Cleavage of C-C Bond in Lignin Models under Visible Light on Mesoporous Graphitic Carbon Nitride through π-π Stacking Interaction. *ACS Catal.* **2018**, *8* (6), 4761−4771.
(47) Rezazadeh, Z.; Soleimani, F.; Mahmoudi, B.; Nasseri, M. A.; Kazemnejadi, M. Facile Synthesis, Characterization, and Antibacterial Activities of CuO, NiO, and Co2O3Metal Oxide Nanoparticles Using Polysalicylaldehyde-Metal Schiff Base Complexes as a Precursor. *Appl. Phys. A: Mater. Sci. Process.* **2021**, *127* (10), 765.
(48) Lee, S. W.; Lee, C.; Goddeti, K. C.; Kim, S. M.; Park, J. Y. Surface Plasmon-Driven Catalytic Reactions on a Patterned Co_3O_4/Au Inverse Catalyst. *RSC Adv.* **2017**, *7* (88), 56073−56080.
(49) Chung, S.-R.; Wang, K.-W.; Sheen, S.-R.; Yeh, C.-T.; Perng, T.-P. Electrochemical Reduction and Hydrogenation of Co Oxides. *Electrochem. Solid-State Lett.* **2007**, *10* (7), A155.
(50) Li, J.; Li, Z.; Zhan, F.; Shao, M. Phase Engineering of Cobalt Hydroxide toward Cation Intercalation. *Chem. Sci.* **2021**, *12* (5), 1756−1761.
(51) Tang, C.-W.; Wang, C.-B.; Chien, S.-H. Characterization of Cobalt Oxides Studied by FT-IR, Raman, TPR and TG-MS. *Thermochim. Acta* **2008**, *473* (1), 68−73.

https://doi.org/10.1021/aps.4c00007
Artif. Photosynth. 2025, 1, 50−62

(52) Ji, W.; Qi, W.; Tang, S.; Peng, H.; Li, S. Hydrothermal Synthesis of Ultrasmall Pt Nanoparticles as Highly Active Electrocatalysts for Methanol Oxidation. *Nanomaterials* **2015**, *5* (4), 2203−2211.
(53) Liu, J.; Zhang, T.; Wang, Z.; Dawson, G.; Chen, W. Simple Pyrolysis of Urea into Graphitic Carbon Nitride with Recyclable Adsorption and Photocatalytic Activity. *J. Mater. Chem.* **2011**, *21* (38), 14398−14401.
(54) Akaike, K.; Aoyama, K.; Dekubo, S.; Onishi, A.; Kanai, K. Characterizing Electronic Structure near the Energy Gap of Graphitic Carbon Nitride Based on Rational Interpretation of Chemical Analysis. *Chem. Mater.* **2018**, *30* (7), 2341−2352.
(55) Zhang, Y.; Yang, Z.; Zheng, D.; Wang, S.; Hou, Y.; Anpo, M.; Zhang, G. Surface Cyano Groups Optimize the Charge Transfer of Poly Heptazine Imide for Enhanced Photocatalytic H2 Evolution. *Int. J. Hydrog. Energy* **2024**, *69*, 372−380.
(56) Zou, Y.; Li, S.; Zheng, D.; Feng, J.; Wang, S.; Hou, Y.; Zhang, G. Extended Light Absorption and Accelerated Charge Migration in Ultrathin Twisted Carbon Nitride Nanoplates for Efficient Solar Hydrogen Production. *Sci. China Chem.* **2024**, *67*, 2215.
(57) Benedet, M.; Rizzi, G. A.; Barreca, D.; Gasparotto, A.; Maccato, C. XPS Analysis of Graphitic Carbon Nitride Functionalized with CoO and CoFe2O4. *Surf. Sci. Spectra* **2023**, *30* (1), 014004.
(58) Cole, K. M.; Kirk, D. W.; Thorpe, S. J. Co3O4 Nanoparticles Characterized by XPS and UPS. *Surf. Sci. Spectra* **2021**, *28* (1), 014001.
(59) Cole, K. M.; Kirk, D. W.; Thorpe, S. J. Co(OH)2 Powder Characterized by x-Ray Photoelectron Spectroscopy (XPS) and Ultraviolet Photoelectron Spectroscopy (UPS). *Surf. Sci. Spectra* **2020**, *27* (2), 024013.
(60) Jiao, J.; Wei, Y.; Chi, K.; Zhao, Z.; Duan, A.; Liu, J.; Jiang, G.; Wang, Y.; Wang, X.; Han, C.; Zheng, P. Platinum Nanoparticles Supported on TiO2 Photonic Crystals as Highly Active Photocatalyst for the Reduction of CO2 in the Presence of Water. *Energy Technol.* **2017**, *5* (6), 877−883.
(61) Trejo-Tzab, R.; Avila-Ortega, A.; Quintana-Owen, P.; Rangel, R.; Álvarez-Lemus, M. A. Platinum-Decorated TiO2: One Step Fast Monometallic Impregnation and Plasma Effect on Nanoparticles. *J. Compos. Sci.* **2022**, *6* (1), 4.
(62) Michel, J. A.; Morris, W. H., III; Lukehart, C. M. Synthesis of Shaped Pt Nanoparticles Using Common Anions or Small Molecules as Shape-Directing Agents: Observation of a Strong Halide or Pseudo-Halide Effect. *J. Mater. Chem. A* **2015**, *3* (5), 2012−2018.
(63) Iervolino, G.; Vaiano, V.; Sannino, D.; Rizzo, L.; Palma, V. Enhanced Photocatalytic Hydrogen Production from Glucose Aqueous Matrices on Ru-Doped LaFeO3. *Appl. Catal. B Environ.* **2017**, *207*, 182−194.
(64) Bellardita, M.; García-López, E. I.; Marcì, G.; Palmisano, L. Photocatalytic Formation of H2 and Value-Added Chemicals in Aqueous Glucose (Pt)-TiO2 Suspension. *Int. J. Hydrog. Energy* **2016**, *41* (14), 5934−5947.
(65) Kumaravel, V.; Imam, M. D.; Badreldin, A.; Chava, R. K.; Do, J. Y.; Kang, M.; Abdel-Wahab, A. Photocatalytic Hydrogen Production: Role of Sacrificial Reagents on the Activity of Oxide, Carbon, and Sulfide Catalysts. *Catalysts* **2019**, *9* (3), 276.
(66) Nwosu, U.; Zhao, H.; Kibria, M.; Hu, J. Unlocking Selective Pathways for Glucose Photoreforming by Modulating Reaction Conditions. *ACS Sustain. Chem. Eng.* **2022**, *10* (18), 5867−5874.
(67) Abbadi, A.; van Bekkum, H. Effect of pH in the Pt-Catalyzed Oxidation of d-Glucose to d-Gluconic Acid. *J. Mol. Catal. Chem.* **1995**, *97* (2), 111−118.
(68) Pasta, M.; Ruffo, R.; Falletta, E.; Mari, C. M.; Pina, C. D. Alkaline Glucose Oxidation on Nanostructured Gold Electrodes. *Gold Bull.* **2010**, *43* (1), 57−64.
(69) Hisatomi, T.; Takanabe, K.; Domen, K. Photocatalytic Water-Splitting Reaction from Catalytic and Kinetic Perspectives. *Catal. Lett.* **2015**, *145* (1), 95−108.
(70) Bi, W.; Li, X.; Zhang, L.; Jin, T.; Zhang, L.; Zhang, Q.; Luo, Y.; Wu, C.; Xie, Y. Molecular Co-Catalyst Accelerating Hole Transfer for Enhanced Photocatalytic H2 Evolution. *Nat. Commun.* **2015**, *6* (1), 8647.
(71) Mankar, A. R.; Pandey, A.; Modak, A.; Pant, K. K. Pretreatment of Lignocellulosic Biomass: A Review on Recent Advances. *Bioresour. Technol.* **2021**, *334*, 125235.
(72) Kuehnel, M. F.; Reisner, E. Solar Hydrogen Generation from Lignocellulose. *Angew. Chem., Int. Ed.* **2018**, *57* (13), 3290−3296.
(73) Zhou, Q.; Feng, F.; Yang, Y.; Zhao, F.; Du, R.; Zhou, Z.; Han, Y. Characterization of a Dextran Produced by *Leuconostoc Pseudomesenteroides* XG5 from Homemade Wine. *Int. J. Biol. Macromol.* **2018**, *107*, 2234−2241.
(74) Keller, M. H.; Moreira, R.; Souza, B. S. Automated Monitoring the Kinetics of Homogeneous and Heterogeneous Chemical Processes Using a Smartphone. *Sci. Rep.* **2022**, *12* (1), 15774.
(75) Gu, Z.; Asakura, Y.; Yin, S. High Yield Post-Thermal Treatment of Bulk Graphitic Carbon Nitride with Tunable Band Structure for Enhanced deNOx Photocatalysis. *Nanotechnology* **2020**, *31* (11), 114001.
(76) Dong, G.; Wen, Y.; Fan, H.; Wang, C.; Cheng, Z.; Zhang, M.; Ma, J.; Zhang, S. Graphitic Carbon Nitride with Thermally-Induced Nitrogen Defects: An Efficient Process to Enhance Photocatalytic H 2 Production Performance. *RSC Adv.* **2020**, *10* (32), 18632−18638.
(77) Niu, P.; Qiao, M.; Li, Y.; Huang, L.; Zhai, T. Distinctive Defects Engineering in Graphitic Carbon Nitride for Greatly Extended Visible Light Photocatalytic Hydrogen Evolution. *Nano Energy* **2018**, *44*, 73−81.
(78) Kuleshov, N. V.; Mikhailov, V. P.; Scherbitsky, V. G.; Prokoshin, P. V.; Yumashev, K. V. Absorption and Luminescence of Tetrahedral Co2+ Ion in MgAl2O4. *J. Lumin.* **1993**, *55* (5), 265−269.
(79) Lim, S.; Ciuparu, D.; Pak, C.; Dobek, F.; Chen, Y.; Harding, D.; Pfefferle, L.; Haller, G. Synthesis and Characterization of Highly Ordered Co-MCM-41 for Production of Aligned Single Walled Carbon Nanotubes (SWNT). *J. Phys. Chem. B* **2003**, *107* (40), 11048−11056.
(80) Hoang, T. V. A.; Nguyen, T. K. A.; Dao, D. Q.; Nguyen, P. A.; Jeong, D. H.; Shin, E. W. Solvent Etching Process for Graphitic Carbon Nitride Photocatalysts Containing Platinum Cocatalyst: Effects of Water Hydrolysis on Photocatalytic Properties and Hydrogen Evolution Behaviors. *Nanomaterials* **2022**, *12* (7), 1188.
(81) Walsh, J. J.; Jiang, C.; Tang, J.; Cowan, A. J. Photochemical CO2 Reduction Using Structurally Controlled G-C3N4. *Phys. Chem. Chem. Phys.* **2016**, *18* (36), 24825−24829.
(82) Godin, R.; Wang, Y.; Zwijnenburg, M. A.; Tang, J.; Durrant, J. R. Time-Resolved Spectroscopic Investigation of Charge Trapping in Carbon Nitrides Photocatalysts for Hydrogen Generation. *J. Am. Chem. Soc.* **2017**, *139* (14), 5216−5224.
(83) Pankratz, J.; Mitchell, E.; Godin, R. Soluble Carbon Nitride Nanosheets as an Alternate Precursor for Hard-Templated Morphological Control. *Nanoscale* **2022**, *14* (37), 13580−13592.
(84) Fu, X.; Long, J.; Wang, X.; Leung, D. Y. C.; Ding, Z.; Wu, L.; Zhang, Z.; Li, Z.; Fu, X. Photocatalytic Reforming of Biomass: A Systematic Study of Hydrogen Evolution from Glucose Solution. *Int. J. Hydrog. Energy* **2008**, *33* (22), 6484−6491.
(85) Zhou, M.; Li, Y.; Peng, S.; Lu, G.; Li, S. Effect of Epimerization of D-Glucose on Photocatalytic Hydrogen Generation over Pt/TiO2. *Catal. Commun.* **2012**, *18*, 21−25.
(86) Nguyen, V.-C.; Ke, N.-J.; Nam, L. D.; Nguyen, B.-S.; Xiao, Y.-K.; Lee, Y.-L.; Teng, H. Photocatalytic Reforming of Sugar and Glucose into H2 over Functionalized Graphene Dots. *J. Mater. Chem. A* **2019**, *7* (14), 8384−8393.
(87) Iervolino, G.; Vaiano, V.; Murcia, J. J.; Rizzo, L.; Ventre, G.; Pepe, G.; Campiglia, P.; Hidalgo, M. C.; Navío, J. A.; Sannino, D. Photocatalytic Hydrogen Production from Degradation of Glucose over Fluorinated and Platinized TiO2 Catalysts. *J. Catal.* **2016**, *339*, 47−56.
(88) Nguyen, V.-C.; Nimbalkar, D. B.; Nam, L. D.; Lee, Y.-L.; Teng, H. Photocatalytic Cellulose Reforming for H2 and Formate Production by Using Graphene Oxide-Dot Catalysts. *ACS Catal.* **2021**, *11* (9), 4955−4967.

https://doi.org/10.1021/aps.4c00007
Artif. Photosynth. 2025, 1, 50−62

(89) Caravaca, A.; Jones, W.; Hardacre, C.; Bowker, M. H2 Production by the Photocatalytic Reforming of Cellulose and Raw Biomass Using Ni, Pd, Pt and Au on Titania. *Proc. R. Soc. Math. Phys. Eng. Sci.* **2016**, *472* (2191), 20160054.
(90) Sanwald, K. E.; Berto, T. F.; Eisenreich, W.; Gutiérrez, O. Y.; Lercher, J. A. Catalytic Routes and Oxidation Mechanisms in Photoreforming of Polyols. *J. Catal.* **2016**, *344*, 806−816.
(91) Yang, B. Y.; Montgomery, R. Alkaline Degradation of Glucose: Effect of Initial Concentration of Reactants. *Carbohydr. Res.* **1996**, *280* (1), 27−45.
(92) Bai, X.; Hou, Q.; Qian, H.; Nie, Y.; Xia, T.; Lai, R.; Yu, G.; Laiq Ur Rehman, M.; Xie, H.; Ju, M. Selective Oxidation of Glucose to Gluconic Acid and Glucaric Acid with Chlorin E6Modified Carbon Nitride as Metal-Free Photocatalyst. *Appl. Catal. B Environ.* **2022**, *303*, 120895.
(93) Liu, Z.; Ma, J.; Hong, M.; Sun, R. Potassium and Sulfur Dual Sites on Highly Crystalline Carbon Nitride for Photocatalytic Biorefinery and CO2 Reduction. *ACS Catal.* **2023**, *13* (3), 2106−2117.
(94) Dong, Y.; Feng, Y.; Li, Z.; Zhou, H.; Lv, H.; Yang, G.-Y. CsPbBr3/Polyoxometalate Composites for Selective Photocatalytic Oxidation of Benzyl Alcohol. *ACS Catal.* **2023**, *13* (21), 14346−14355.

https://doi.org/10.1021/aps.4c00007
Artif. Photosynth. 2025, 1, 50−62